Applied Catalysis A: General 348 (2008) 153–164

Microstructural characterization of $Cu/ZnO/Al_2O_3$ catalysts for methanol steam reforming - A comparative study

P. Kurr[a,b], I. Kasatkin[a], F. Girgsdies[a], A. Trunschke[a], R. Schlögl[a] T. Ressler[b]*

[a]Department of Inorganic Chemistry, Fritz-Haber-Institute of the Max-Planck-Society, Faradayweg 4-6, 14195 Berlin, Germany
[b]Institute of Chemistry, Technical University Berlin, C-2, Straße des 17. Juni 135, 10623 Berlin, Germany

* Corresponding author: e-mail thorsten.ressler@tu-berlin.de, Tel.: +49 30 314 79736; fax: +49 30 314 21106

Received 17 March 2008; revised 30 May 2008; accepted 9 June 2008. Available online 22 June 2008.

Abstract

Microstructural characteristics of various *real* $Cu/ZnO/Al_2O_3$ catalysts for methanol steam reforming (MSR) were investigated by *in situ* X-ray diffraction (XRD), *in situ* X-ray absorption spectroscopy (XAS), temperature programmed reduction (TPR) and electron microscopy (TEM). Structure–activity correlations of binary Cu/ZnO model catalysts were compared to microstructural properties of the ternary catalysts obtained from *in situ* experiments under MSR conditions. Similar to the binary system, in addition to a high specific copper surface area the catalytic activity of $Cu/ZnO/Al_2O_3$ catalysts is determined by defects in the bulk structure. The presence of lattice strain in the copper particles as the result of an advanced Cu–ZnO interface was detected only for the most active $Cu/ZnO/Al_2O_3$ catalyst in this study. Complementarily, a highly defect rich nature of both Cu and ZnO has been found in the short-range order structure (XAS). Conventional TPR and TEM investigations confirm a homogeneous microstructure of Cu and ZnO particles with a narrow particle size distribution. Conversely, a heterogeneous microstructure with large copper particles and a pronounced bimodal particle size distribution was identified for the less active catalysts. Apparently, lattice strain in the copper nanoparticles is an indicator for a homogeneous microstructure of superior $Cu/ZnO/Al_2O_3$ catalyst for methanol chemistry.

Keywords: Methanol steam reforming; $Cu/ZnO/Al_2O_3$ catalyst; Hydrogen production; Homogeneous microstructure; Cu lattice strain; TPR; TEM; XRD; XAS; *In situ*

1. Introduction

Cu-catalysts supported on $ZnO–Al_2O_3$ mixed oxides are of considerable industrial interest for low-pressure methanol synthesis and water-gas shift reaction (WGS). They are also known to be active in methanol steam reforming (MSR). Methanol, as a chemical carrier of hydrogen to be applied in fuel cells is a promising alternative for petroleum-based fuels [1]. Especially low temperature fuel cells such as proton exchange membrane (PEM) fuel cells for small-scale applications impose high purity requirements of the hydrogen since the electrodes are very sensitive to poisoning by several contaminants (CO, sulfur) [2] and [3]. Integration of a supported membrane with a steam reformer exhibits considerable promise for generating high purity hydrogen [4]. Desired Cu based steam reforming catalysts combine high activity with high selectivity towards hydrogen even at moderate temperatures (473–573 K). Moreover, they show a suitable chemical and thermal stability. In order to elucidate synthesis pathways to the active *real* structure, a fundamental understanding of the relation between both bulk and surface structure and the catalytic performance is required (*structure–activity relationship*).

It is generally accepted that a high copper surface area is a prerequisite for superior $Cu/ZnO(Al_2O_3)$ catalysts in methanol chemistry. Deviations from a linear correlation between copper metal surface area and catalytic activity have been frequently reported in the recent literature on Cu based Zn-, Al-oxides [5], [6], [7], [8] and [9]. Hence, additional parameters such as geometric and electronic defects on the surface and/or in the bulk also determine the catalytic performance of copper catalysts in methanol chemistry. Recently we have shown that methanol steam reforming and methanol synthesis activities of binary Cu/ZnO model

catalysts with varying molar ratios of the metals correlate with lattice strain in the copper particles [6] and [10]. Ultraviolet photoelectron spectroscopy (UPS) investigations on thin copper films on silicon model systems revealed that thermally induced strain indeed influences the Cu d band and, hence, the electronic structure of the surface [11]. Moreover, microstructural investigations of Cu/ZnO catalysts for MSR by *in situ* XRD, *in situ* XAS, ^{63}Cu NMR as well as HRTEM revealed a positive correlation between strained copper particles and a homogeneous microstructure of the final catalyst. The characteristic defect structure is accompanied by an improved catalytic performance in steam reforming of methanol [12], [13] and [14]. Lattice strain in the copper phase as the result of an intimate Cu–ZnO interface is an indicator of a homogeneous microstructure of superior Cu/ZnO catalysts [13].

The more complex ternary $Cu/ZnO/Al_2O_3$ catalysts are currently industrially established for low pressure and temperature regimes in methanol chemistry (steam reforming, synthesis) and in the WGS reaction. The solid-state chemistry of the preparation and structure–activity correlations are highly complex. Compared to the role of ZnO as a structural promoter in $Cu/ZnO/Al_2O_3$ catalysts [12], [13], [14], [15], [16], [17], [18], [19], [20] and [21], alumina is known to inhibit thermal sintering of metal particles and, therefore, imparts chemical and thermal stability required for an industrially used catalyst [22], [23] and [24]. The precursor preparation is governing the electronic and structural properties of the final copper catalyst (*chemical memory* effect [25]). Here we present microstructural and catalytic characteristics of various laboratory prepared ternary $Cu/ZnO/Al_2O_3$ catalysts under MSR conditions. A commercial $CuO/ZnO/Al_2O_3$ methanol synthesis catalyst was employed for comparison. Complementary *in situ* bulk techniques, X-ray diffraction (XRD), and X-ray absorption spectroscopy (XAS), were used for bulk structural investigations of $Cu/ZnO/Al_2O_3$ catalysts under working conditions in methanol steam reforming. Microscopic and morphological characteristics of the local structure were examined by electron microscopy (TEM). It will be shown that microstructural characteristics found for the binary Cu/ZnO system also holds for the ternary $Cu/ZnO/Al_2O_3$ catalysts. The highly defect rich, non-ideal crystalline nature of Cu and ZnO species in a ternary catalyst behaves similar to that of binary Cu/ZnO model systems. Thus, correlations found for the binary system are applicable to the more complex ternary $Cu/ZnO/Al_2O_3$ system.

2. Experimental

2.1. Sample preparation

Various CuZnAl-mixed oxide precursors (CZA) were prepared on a laboratory scale according to patented procedures. Hydroxycarbonates were precipitated from metal nitrate solutions and subsequently washed, dried and calcined. All chemicals employed were obtained from *Fluka Chemicals* and were used without further purification.

CZA-1: A commercial $Cu/ZnO/Al_2O_3$ catalyst for methanol synthesis provided by *Süd-Chemie AG* was employed as reference.

CZA-2: 3600 g $Cu(NO_3)_2{\cdot}3H_2O$, 733 g $Zn(NO_3)_2{\cdot}6H_2O$ and 2089 g $Al(NO_3)_3{\cdot}9H_2O$ were dissolved in 15 l of deionized water. A solution of 2500 g $(NH_4)_2CO_3$ in 63.5 l deionized water was employed as precipitation reagent. The precipitation process occurred at 303 K under vigorous stirring (dosing rate: 2.2 l min^{-1}). The entire basic solution was added in about 30 min and the final pH-value of the suspension was adjusted to 6.8 ± 0.1. The precipitate was aged in the mother liquid for 2 h, filtered off, washed, and dried in a drying oven at 393 K for 36 h. Finally, the precursor material was calcined at 673 K for 2 h [26].

CZA-3: The preparation sequence used was similar to that of sample CZA-2 (precipitating, washing, calcination). Unlike sample CZA-2, a different drying procedure was applied (spray drying of a 5 wt.% suspension).

CZA-4: 5.8 g $Cu(NO_3)_2{\cdot}3H_2O$, 1 g $Zn(NO_3)_2{\cdot}6H_2O$ and 3.53 g $Al(NO_3)_3{\cdot}9H_2O$ were dissolved in 1 l of deionized water. A premixed solution of 53 g Na_2CO_3 in 1 l deionized water was added under vigorous stirring at ambient temperature (dosing rate: 2.5 l min^{-1}). The resulting precipitate was repeatedly washed to remove sodium ions. The solid phase was recovered by filtration, dried at 353 K for 12 h, and finally calcined at 573 K for 1 h [27].

CZA-5 + CZA-6: Additionally, sample CZA-4 was 45 times (CZA-5) and 225 times (CZA-6) up scaled.

The amount of copper, zinc, and aluminum in the prepared catalysts was determined by X-ray fluorescence analysis (XRF). About 50 mg of calcined catalyst was used in the analysis of each sample. The accuracy obtained was estimated to be ±1%.

2.2. Activity screening

In order to achieve comparable reaction conditions for all CZA catalysts a standard procedure of catalyst handling was applied. An amount of 300 mg of a homogeneous mixture (sieve fraction 300–450 μm) of 50 mg of the CZA catalyst and 250 mg of hexagonal boron nitride (BN, *Alfa Aesar*) was placed into a fixed-bed micro reactor consisting of a quartz tube (7 mm i.d.) with a thermocouple located in the catalyst bed. The activity measurements were conducted in the following sequence for all CZA catalysts. Prior to each experiment the catalyst was activated by heating in 5 vol.% H_2 in He (80 ml min^{-1}) to 523 K with a temperature ramp of 6 K min^{-1} and an isothermal period of 1 h at 523 K before cooling down to room temperature. Methanol and water were supplied by saturating He carries in two sets of saturators ($T_{Saturator}$ = 298 K). The reactor feed contained 3.5 vol.% water, 3.5 vol.% methanol, and balance helium. Total flow was kept at 100 ml min^{-1} by mass flow controllers. Catalytic activity in MSR was measured at

523 K (heating rate: 6 K min^{-1}) by on-line GC analysis (*Varian* MicroGC 4900) equipped with a TCD detector using a PPU column and a Molsieve 5 Å column for separating polar products, such as water, methanol and CO_2 and the gaseous products, such as H_2, He, and CO, respectively. Steady-state activities of the catalysts were determined 8 h after changing to reaction conditions. The catalysts exhibited typical deactivation behavior during the first 4 h time on stream. Subsequently, no significant loss in activity was detected over a period of 8 h. A blank run conducted with an empty reactor did not show any detectable activity. Selectivities were calculated at the basis of carbon.

2.3. Specific Cu surface area determination

The specific Cu^0 surface area of the catalysts was measured by the dissociative chemisorption of nitrous oxide (N_2O-RFC [28]). The experiments were performed in quartz micro-reactor at 303 K to avoid subsurface oxidation [29]. Prior to each experiment the catalysts was reduced in 5 vol.% H_2 (He) at 523 K. Subsequently, the reactor was purged for 1 h with He and cooled down to ambient temperature to achieve an adsorbate-free reduced Cu surface. The measurement was started by switching from pure He to 1 vol.% N_2O in He (*Messer Griesheim*) by means of a four way valve. The evolved gas atmosphere was monitored using a quadrupole mass spectrometer (*OMNISTAR, Pfeiffer*). The amount of nitrogen formed was quantified from the time interval of the frontal chromatogram of N_2 (i.e. the time interval between the onset of appearance of N_2 and the breakthrough of N_2O). The Cu surface area was calculated assuming a molar stoichiometry of $Cu_s/N_2 = 2$ and a value of 1.46×10^{-19} copper atoms m^{-2} [30].

2.4. Temperature programmed reduction

Temperature programmed reduction (TPR) studies have been conducted on a TPD/R/O 1100 instrument (*CEInstruments*). TPR studies were carried out by passing 5 vol.% H_2 (Ar) at a flow of 80 ml min^{-1} over 50 mg of the catalyst sample contained in a quartz tube. The temperature was increased to 523 K with a heating ramp of 6 K min^{-1} and maintained isothermal for 1 h. Hydrogen consumption was calculated quantitatively from the integrated TPR signal, calibrated with CuO (*Sigma–Aldrich*) as a standard. The TPR studies were performed according to the criterion of *Monti & Baiker* [31] and *Maleta & Caballero* [32]. Prior to a measurement the sample was purged in an argon flow (10 ml min^{-1}) up to 423 K to ensure an adsorbate-free surface.

2.5. Transmission electron microscopy

Immediate transfer of the reduced catalyst into a glove box prevented exposure to air. The samples were dispersed in acetone and deposited on a vacuum transfer sample holder. High-resolution transmission electron microscopy (HRTEM) experiments of the reduced catalysts were performed on a *Philips* CM 200 FEG microscope equipped with a *Gatan* imaging filter operating at 200 kV (C_s = 1.35 mm). The information limit was better than 0.18 nm. The experimental micrographs were digitalized using a CCD camera. In addition to the computed images, selected areas were processed to obtain their power spectra (PS) which is the square of the Fouriertransform of the image. The power spectra were used for measuring net-plane distances (±0.5%) and angles (±0.5 degree) for phase identification.

2.6. In situ X-ray diffraction

In situ X-ray diffraction experiments were performed on a *STOE* Theta/Theta diffractometer (Cu Kα radiation, secondary monochromator, scintillation counter) operating at 50 kV and 30 mA in a reflection scan mode. The diffractometer was equipped with a *Paar* XRK 900 high temperature cell. 80 mg of the calcined catalyst precursor were used for *in situ* measurements. XRD patterns were recorded at 523 K in reducing atmosphere (5 vol.% H_2) and under MSR conditions (3.5 vol.% methanol, 3.5 vol.% water). XRD pattern were measured in the 2θ range from 10° to 100° with a step size of 0.04° and a time/step of 2 s. The gases were pre-mixed by mass flow controllers and introduced in the reaction cell with a total flow of 150 ml min^{-1}. The gas phase composition was monitored using a *Pfeiffer* quadrupole mass spectrometer (*OMNISTAR*).

Microstructural changes of the $Cu/ZnO/Al_2O_3$ catalyst under working conditions were elucidated by a detailed line profile analysis of the X-ray diffraction patterns. With a sum of pseudo-*Voigt*-profile functions and an appropriate background function (polynomial 3rd degree) X-ray diffraction pattern were refined [33]. Diffraction line profile analysis was conducted by means of the integral breath method for size and lattice strain (*Pawley* method). This is reasonable because trends in microstructural changes can be identified by comparing a series of similar treated catalysts [34]. Refined parameters were lattice constants, peak intensities, *Lorentzian* and *Gaussian* parts of the profile of each individual *h k l* line, a linear zero shift in the 2θ scale and four coefficients for the background polynomial. A correction for instrumental broadening was omitted because the full width at half maximum (FWHM) of each peak is more than ten times the instrumental broadening.

Table 1: Methanol conversion and product composition for methanol steam reforming over various $Cu/ZnO/Al_2O_3$ (CZA) catalysts determined in a fixed-bed reactor (reaction temperature 523 K; ambient pressure; catalyst mass 0.05 g; total gas flow rate 100 ml min^{-1}; feed concentration: 3.5 vol.% CH_3OH + 3.5 vol.% H_2O)

Sample	Methanol conversion (%)	Product composition (%)			H_2 production rate ($\mu mol\ s^{-1}\ m_{Cu}^{-2}$)
		CO_2	H_2	CO	
CZA-1	84.4	24.67	75.23	0.11	130
CZA-2	43.4	24.90	75.02	0.08	204
CZA-3	59.5	25.02	74.90	0.08	166
CZA-4	57.8	24.95	74.92	0.13	176
CZA-5	25.4	24.91	74.97	0.13	142
CZA-6	16.2	25.82	74.07	0.10	74

2.7. In situ X-ray absorption spectroscopy

In situ X-ray absorption spectroscopy experiments were performed at the Hamburg synchrotron radiation laboratory, HASYLAB, at beamline X1 (Germany) at the Cu K-edge (E = 8979 eV) and the Zn K-edge (E = 9659 eV) in the transmission mode. 3 mg of the catalyst precursor and 30 mg BN (<325 mesh, *Alfa Aesar*) were physically mixed and pressed at a force of 1 ton into a pellet with 5 mm in diameter. The amount of material in the pellets was calculated to yield an absorber optical thickness of about 1.5 absorption lengths. Catalytic activity in methanol steam reforming was determined as described above. The gas phase composition was analyzed by mass spectrometry (*OMNISTAR*, *Pfeiffer*). Analysis of the XAS spectra was performed with the software package *WinXAS 3.1* [35]. A general data analysis procedure of the measured absorption spectra consists of energy calibration according to a copper reference foil, background subtraction by using two polynomials, and normalization. After transformation into the k space, an atomic background $\mu_0(k)$ was determined using a cubic spline function. The pseudo radial distribution function (RDF) was obtained by Fourier transformation of the k^3 weighted experimental spectrum $\chi(k)$ (k range from 3 $Å^{-1}$ to 13 $Å^{-1}$ for Cu K-edge and from 3 $Å^{-1}$ to 11.9 $Å^{-1}$ for Zn K-edge) multiplied by a Bessel window into the R space. Theoretical backscattering phases and amplitudes for single and multiple scattering paths were calculated up to 6 Å for cubic Cu metal, monoclinic CuO, and hexagonal ZnO using the *ab-initio* multiple-scattering code *FEFF 7* [36]. Refinement of the Cu, CuO, and ZnO model structure to the experimental EXAFS spectrum by a least-squares method was conducted in the R space. Structural parameters refined were the single scattering shell distances (R), the *Debye–Waller* factors of the single scattering paths (σ^2), and one overall E_0 shift. The coordination numbers (CN) were kept invariant because of the rather large Cu, CuO, and ZnO crystallite sizes.

3. Results

3.1. Catalytic activity in methanol steam reforming

The steady-state activities measured for all catalysts in MSR are summarized in Table 1. Steam reforming of methanol over $Cu/ZnO/Al_2O_3$ catalysts resulted in the formation of hydrogen and carbon dioxide in a ratio of 3:1 under the experimental conditions used. CO was most likely produced by reverse WGS reaction [37]. Other by-products such as formaldehyde, formic acid, methyl formate, and dimethyl ether formed during reaction of methanol on $Cu/ZnO/Al_2O_3$ catalysts could not be detected under the reaction conditions applied [38]. The trends in activity measured in the micro-reactor are also reflected in the *in situ* experiments (Fig. 1). For comparison, the methanol conversion was determined for all experiments at constant reaction temperature (523 K) and similar space velocities ($WHSV_{MeOH}$ = [86–96] s^{-1}). Overall methanol conversions determined in the *in situ* cells were approximately 5–10% for the *in situ* XAS experiments and 15–30% for the *in situ* XRD experiments. The equilibrium conversion of methanol in MSR calculated according to *Hess's* law from the standard formation enthalpies and entropies of the involved substances [39] under the conditions employed amounts to nearly 99% ($X^{Equilibrium}$ = 98.8%). The *in situ* measurements were performed under differential conditions in the kinetically controlled regime. Thus, it can be concluded that the *in situ* experiments permit deducing reliable structure–

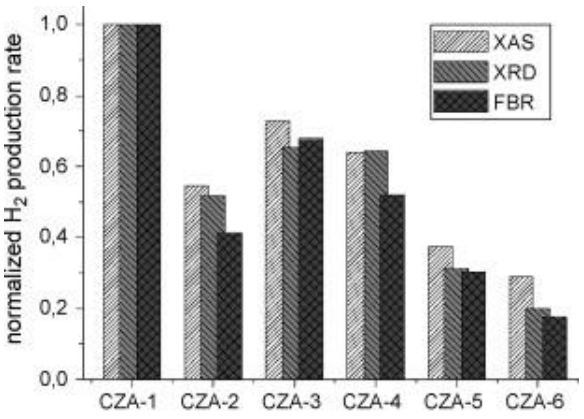

Fig. 1: Comparison of the normalized H_2 production rates obtained from *in situ* experiments (XRD, XAS) and measured in a fixed bed micro-reactor (FBR) at 523 K, $WHSV_{MeOH}$ = (86–92) s^{-1}.

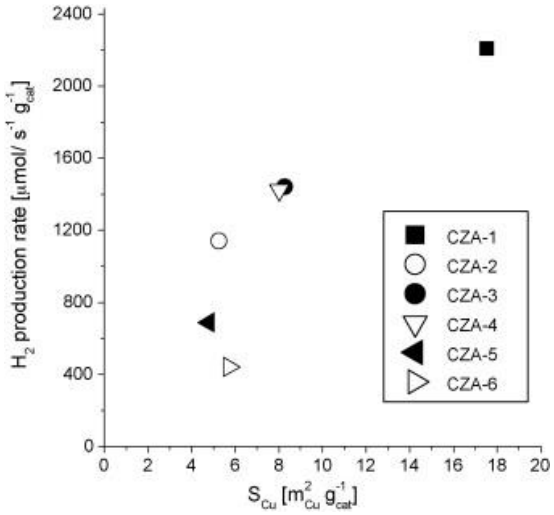

Fig. 2: H_2 production rate obtained in a fixed-bed reactor in dependence on the specific copper surface area determined by N_2O surface titration (RFC).

activity relationships. Moreover, a similar trend in the reaction rate was found for the catalyst series in methanol synthesis (*principle of microscopic reversibility*, data not shown).

The catalytic activity measured is mainly determined by the specific copper surface area (Fig. 2). For the catalysts studied, hydrogen production rate per gram catalyst appears to increase with the Cu surface area (Fig. 2). Best performance in MSR in terms of Methanol conversion was determined for CZA-1 exhibiting the highest accessible Cu surface area and highest Cu dispersion (Table 3). Contrarily, this sample did not exhibit the highest intrinsic activity in MSR reaction. The intrinsic activity—the H_2 production rate per m_{Cu}^2 of sample CZA-1 is roughly half of sample CZA-2 (see Table 1). The lowest activity was determined for the sample CZA-6 (5.7 m_{Cu}^2 g_{Cat}^{-1}). Interestingly, this catalyst exhibited a similar Cu surface area than the much more active catalyst CZA-2 (see Fig. 2). The activity of sample CZA-2 is roughly three times that of CZA-6 (Table 1).

3.2. General characterization of the CZA catalysts (TPR and TEM)

The bulk metal compositions of all investigated catalysts examined by X-ray fluorescence spectroscopy are given in Table 2. Different Zn and Al contents were found for the various CZA catalysts whereas the copper loadings (62–65 wt.%) are relatively similar. The overall Cu/Zn ratio in the catalysts investigated has been confirmed by XAS (see Table 2).

Table 2: Metal composition of the investigated CZA catalysts determined by X-ray fluorescence analysis (XRF) and Cu to Zn ratio determined from the edge jump at the Cu K and the Zn K-edge (XAS)

Sample	Cu (wt.%)	Zn (wt.%)	Al (wt.%)	Cu/Zn ratio[a]	Cu/Zn ratio[b]
CZA-1	61.7	29.7	8.6	2.08	2.35
CZA-2	65.1	18.0	16.7	3.62	3.57
CZA-3	64.5	17.1	18.4	3.77	3.80
CZA-4	62.5	17.2	20.3	3.64	3.64
CZA-5	62.3	14.8	22.9	4.21	4.18
CZA-6	65.0	10.6	24.4	6.13	6.05

Fig. 3 compares the hydrogen consumption profiles during temperature programmed reduction of the $CuO/ZnO/Al_2O_3$ precursors. All investigated oxide precursors showed an onset of reduction between 423 K and 453 K. The maxima of the reduction peaks obtained are located at about 483–523 K (Fig. 3). A quantitative analysis of the hydrogen consumption revealed that a complete reduction to metallic copper for all samples was achieved. These calculations presume that all Cu in the oxide precursor was bivalent. Pure CuO is reduced at considerably higher temperature (563 K). Pure ZnO and alumina are not reduced under these conditions [40]. The reduction of CZA-1 is completed at the lowest reduction temperature of all catalysts studied. The characteristic TPR profile and the peak maximum temperature of 498 K indicate a homogeneous size distribution of CuO particles. This result correlates well with the measured specific Cu^0 surface area, where the highest dispersion was found for the CZA-1 catalyst (Table 3). A very different behavior was found for the other catalysts. The TPR profiles of CZA-2–6 are considerable broader and shifted to higher reduction temperatures. Moreover, the reduction profiles of CZA-2, CZA-4–6

Table 3: Specific Cu surface area (S_{Cu}) determined by N_2O frontal chromatography (RFC), and structural characteristics of the reduced $Cu/ZnO/Al_2O_3$ catalysts determined by XRD: Cu crystallite size (D_{Cu}), Cu lattice strain (ε_{Cu}), and Cu dispersion (d_{Cu})

Sample	S_{Cu} ($m_{Cu}^2\ g_{Cat}^{-1}$)[a]	D_{Cu} (Å)[b]	S_{Cu} ($m_{Cu}^2\ g_{Cat}^{-1}$)[lk and lk]	ε_{Cu} (%)[b]	d_{Cu} (%)
CZA-1	17.5	51	17.2	0.39	4.9
CZA-2	5.3	45	20.1	–	1.5
CZA-3	8.3	54	16.4	–	2.4
CZA-4	8.0	65	17.9	–	1.8
CZA-5	4.8	73	14.5	–	1.1
CZA-6	5.7	77	14.4	–	1.4

[a] Determined by RFC.
[b] Calculated from XRD pattern line broadening of most prominent Cu(1 1 1) reflection.
[c] Assuming hemisphere like Cu particles on the surface.

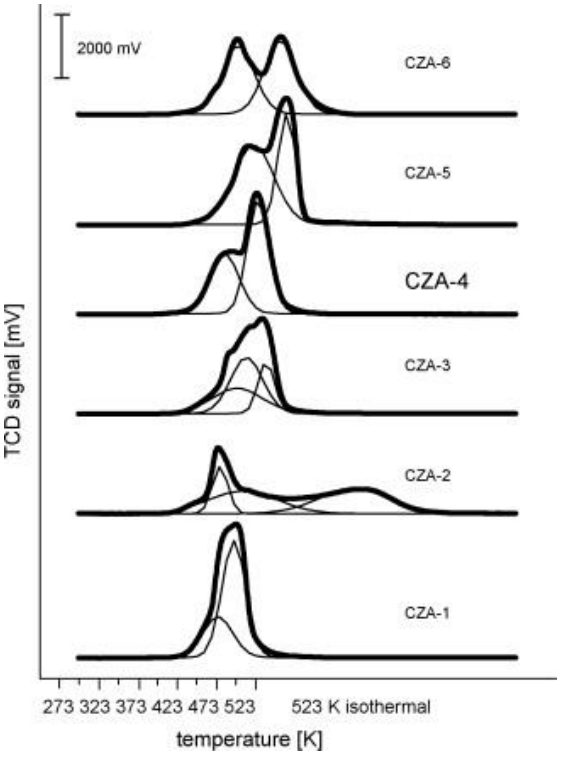

Fig. 3: Hydrogen consumption during temperature programmed reduction (TPR) of the CZA catalysts. Bold lines are experimental curves and thin lines are deconvoluted curves.

showed two or even three regions of reduction. While a small reduction peak is observed at a similar temperature like sample CZA-1 – with the maximum between 483 K and 498 K – most of the reduction occurred during the isothermal period of the reduction at 523 K (see Fig. 3).

Fig. 4 shows transmission electron micrographs (scale bars: 100 and 20 nm, respectively) of the samples CZA-1, 2, and 4 after reduction in hydrogen. Electron energy loss spectroscopy (EELS) identified only metallic Cu as copper phase in all samples studied. However, HRTEM analysis of selected areas evidences the presence of minute amounts of Cu_2O, brass, ZnO_{1-x} and amorphous materials in addition to the main phases: Cu and ZnO. Aluminum was hardly detected and mainly found as amorphous phase. In rare cases Al has been identified as crystalline α-Al_2O_3 by HRTEM. Various morphologies of Cu and ZnO particles were detected for the $Cu/ZnO/Al_2O_3$ catalysts, such as round and irregular shaped Cu particles as well as plate and needle like ZnO particles (Fig. 4a–f). In contrast to sample CZA-1, large copper particles (up to 150 nm) were found for CZA-2–6 catalysts. The distinct bimodal particle size distribution that is visible from the micrographs in Fig. 4 is in accordance with TPR results (see Fig. 3). High-resolution electron micrographs of a *good* (CZA-1) as well as of a *very poor* catalyst (CZA-5) obtained after reduction are depicted in Fig. 5 (scale bars: 10 and 5 nm). The HRTEM images of the CZA-1 catalyst exhibited a marked interface between the Cu and ZnO particles (Fig. 5a). The majority of Cu particles were round-shaped and the surfaces of the metal particles were often covered with smaller ZnO particles (Fig. 5a). The particles were relatively homogeneous, small-sized, and exhibited a Gaussian like size distribution with a mean value of 11 nm for Cu and 7 nm for ZnO. Conversely, in sample CZA-5 small rounded Cu particles are embedded in an amorphous matrix. Sintering of Cu particles in various orientations resulted in dislocations at the interface (see Fig. 5b). A characteristic Cu–ZnO interface such as that found in CZA-1 catalyst (Fig. 5a) was not detected in the CZA-5 catalysts.

3.3. Bulk structural in situ investigations (XRD, XAS)

The bulk structure of copper in the various ternary $Cu/ZnO/Al_2O_3$ catalysts was studied under reduction and steam reforming conditions by *in situ* XRD. The XRD

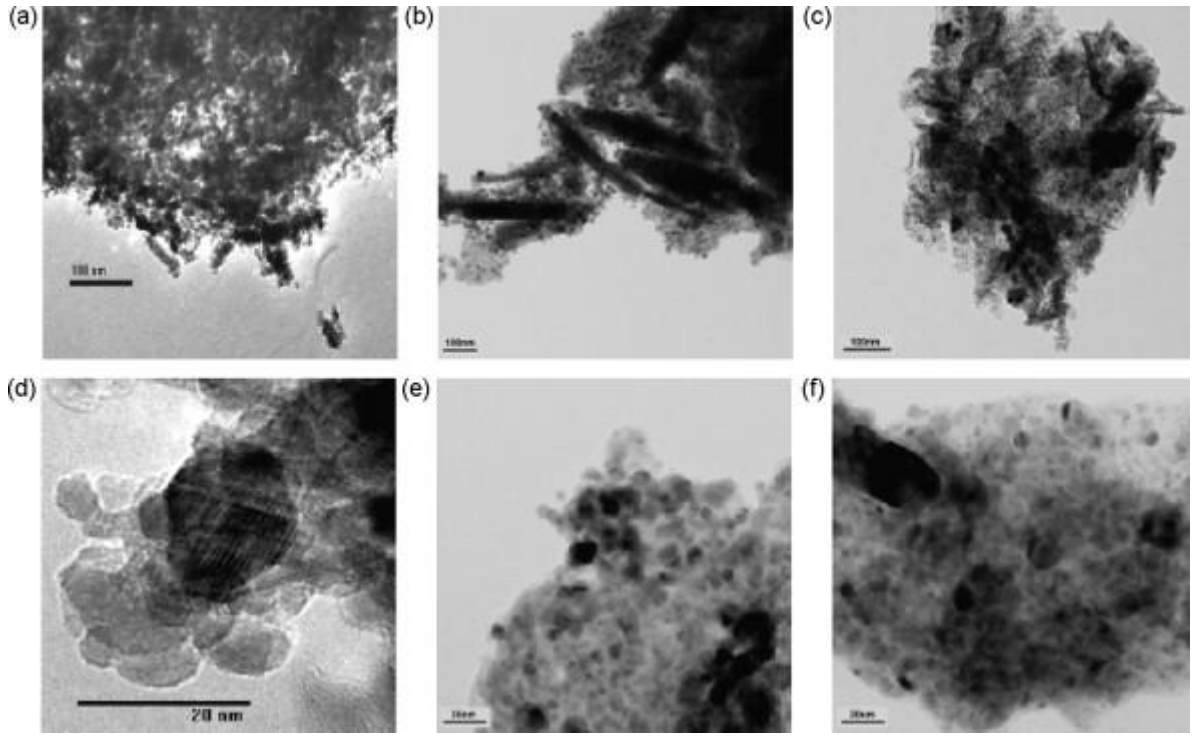

Fig. 4: Bright field transmission electron micrographs of the activated $Cu/ZnO/Al_2O_3$ catalysts with different magnifications (scale bars: 100 and 20 nm): (a) + (d) CZA-1, (b) + (e) CZA-2, (c) + (f) CZA-4.

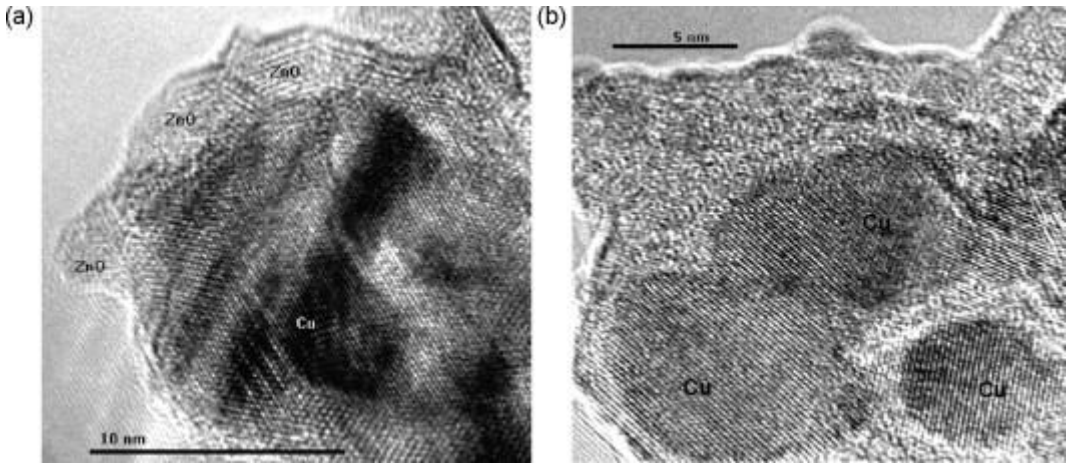

Fig. 5: High-resolution electron micrograph of the sample (a) CZA-1 and (b) CZA-5 after activation in hydrogen (scale bars: 10 and 5 nm).

powder patterns of the calcined precursors are depicted in Fig. 6a. All precursors showed broad diffraction lines corresponding to monoclinic CuO (ICDD-PDF 45-937). ZnO appeared to be almost X-ray amorphous. Only for the sample CZA-1 diffraction lines of ZnO (ICDD-PDF 36-1451) were present. For samples CZA-2–6 there is an increased background in the 2θ region between 30° and 37° which indicates the presence of either highly nano-crystalline or X-ray amorphous ZnO (Fig. 6a). Crystalline Rosasite {$(Cu, Zn)_2CO_3(OH)_2$; ICDD-PDF 36-1475} is clearly observed for sample CZA-1 at lower 2θ angles (see Fig. 6a). On-line MS analysis of the evolved gas atmosphere during the reduction of the calcined precursors revealed that the oxide precursors of samples CZA-2–6 also contained residual OH^- and Co_3^{2-}. In contrast to CZA-1 the corresponding components appeared to be X-ray amorphous for the other CZA oxide precursors (see Fig. 6a). No diffractions lines corresponding to Al compounds were observed. This suggests that the Al compounds were either amorphous or highly dispersed in the catalysts. After reduction in hydrogen, CuO is completely reduced to copper metal as it can be deduced from XRD (Fig. 6b). The XRD pattern of the reduced catalysts can be very well simulated by a mixture of hexagonal ZnO and cubic Cu. A *Rietveld* refinement of the corresponding ICSD model structures to the experimental pattern resulted in a phase composition of ~70–80%

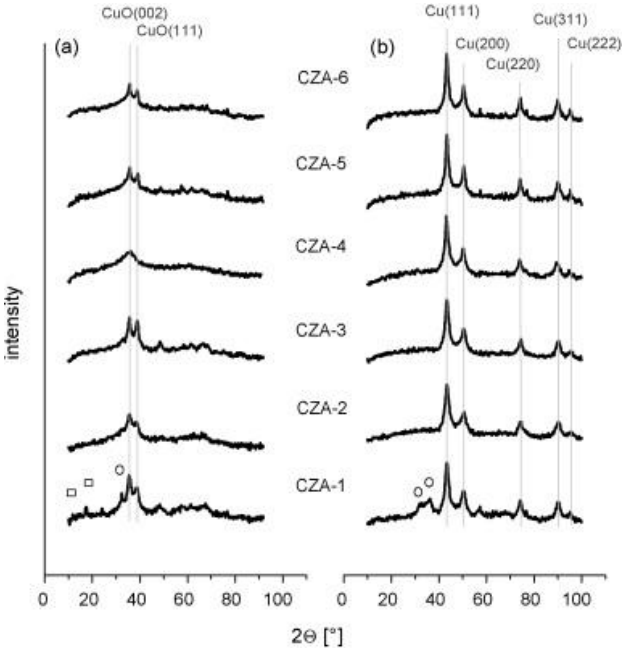

Fig. 6: *In situ* powder X-ray diffraction patterns recorded at ambient temperature of the (a) calcined precursors, and (b) of the reduced catalysts (○ ZnO; □ Rosasite {$(Cu,Zn)_2CO_3(OH)_2$}).

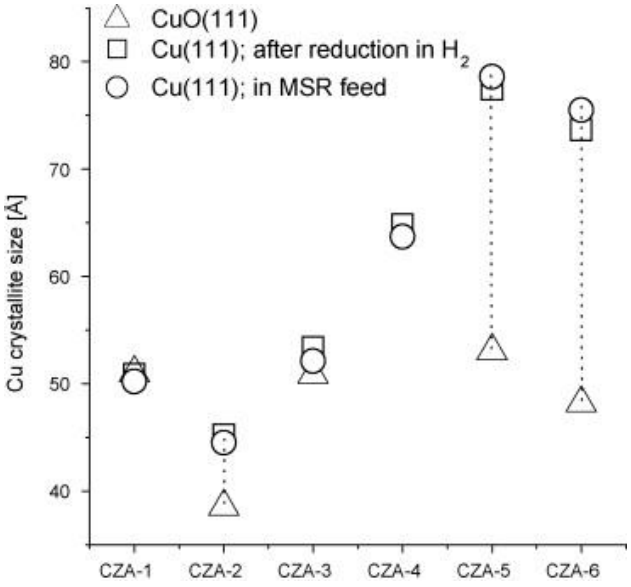

Fig. 7: Crystallite sizes of CuO and Cu determined from the XRD line broadening of the calcined precursor, the reduced and the catalyst under MSR conditions.

cubic Cu and ~20–30% hexagonal ZnO. All catalysts exhibited broad diffraction lines corresponding to cubic Cu metal (ICDD-PDF 4-836). Bulk structural parameters such as Cu crystallite size and Cu lattice strain after reduction are given in Table 3. The averaged Cu crystallite sizes calculated from line broadening of Cu(1 1 1) reflection range from 45 Å to 80 Å. However, in the set of catalysts studied, only the sample CZA-1 exhibited lattice strained Cu particles (Table 3). Exposure to the steam reforming feed had no significant influence on the diffraction pattern and the corresponding bulk structural characteristics, such as phase composition, crystallite size, and lattice strain. The lattice constants are in agreement with ideal crystalline *fcc* Cu (Table 4). Accordingly, the absorption edge position determined as the position of the inflection point of the Cu K-edge absorption spectra of the reduced CZA catalysts matches with bulk Cu^0 (Table 4). The copper phase crystallite sizes determined from the integral breadth of the CuO(1 1 1) and Cu(1 1 1) reflections after the various treatments (i.e. calcined precursor, reduced catalysts, and catalyst under MSR conditions) are summarized in Fig. 7. A comparison of the crystallite sizes before and after reduction revealed that during the reduction process the crystallite sizes for the samples CZA-2 and especially for CZA-5 and 6 increased. Due to the highly amorphous XRD spectra of sample CZA-4 in the calcined state no CuO crystallite sizes have been calculated (see Fig. 6a). Conversely, no changes in crystallite size were determined for the CZA-1 catalyst. Exposure to the steam reforming feed had no significant influence on the crystallite size for any of catalysts investigated (see Fig. 7).

Analysis of the extended fine structure of the experimental spectra (EXAFS) measured under reaction conditions at the Cu K-edge and Zn K-edge revealed changes in the short-range order structure of the catalysts. The resulting pseudo radial distribution functions at the Cu K-edge, FT($\chi(k)\cdot k^3$), after reduction of all catalysts are depicted in Fig. 8. Deviations of the FT($\chi(k)\cdot k^3$) of the various catalysts were most pronounced for the amplitude of the 1st Cu–Cu shell (R < 3 Å). This has been also found for the spectra recorded in MSR feed under reaction conditions (see σ_{Cu}^2 in Table 4). MSR activities determined in the XAS cell coincided

Table 4: Comparison of Cu lattice constant a (*in situ* XRD), Cu K-edge position E_0, Cu–Cu distance R, and the *Debye–Waller* factor (σ_{Cu}^2) obtained from fitting theoretical *fcc* Cu to the experimental EXAFS of the 1st Cu–Cu shell (*in situ* XAS) under working conditions (feed, 523 K)

Sample	a_{Cu} XRD (Å)[a]	E_0 (keV)[b]	R 1st Cu–Cu (Å)	σ^2 1st Cu–Cu (Å^2)
CZA-1	3.615	8.978(7)	2.53	0.0170
CZA-2	3.615	8.978(7)	2.54	0.0176
CZA-3	3.615	8.978(6)	2.53	0.0168
CZA-4	3.615	8.978(6)	2.53	0.0199
CZA-5	3.614	8.978(7)	2.54	0.0187
CZA-6	3.615	8.978(8)	2.53	0.0184

[a] $a(Cu_{fcc})$ = 3.615 Å (ICDD-PDF 4-836).
[b] Energy offset determined as the position of the inflection point of the continuum curve ($E_0(Cu_{fcc})$ = 8.979 keV).

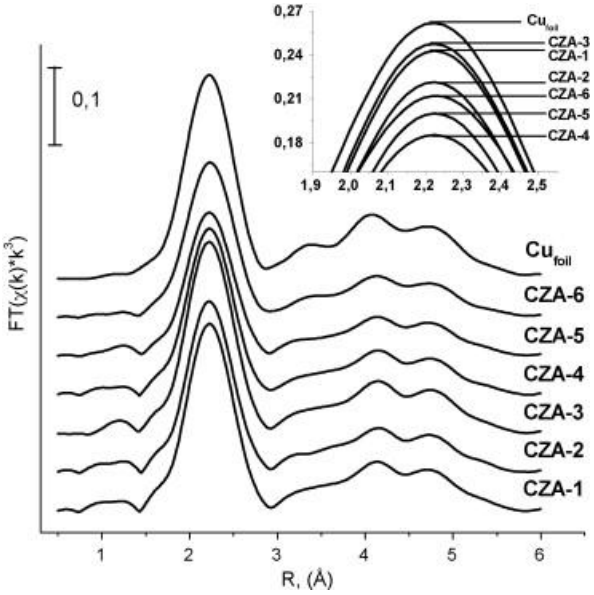

Fig. 8: Experimental Cu K-edge FT($\chi(k)\cdot k^3$) of the in 5 vol.% H_2(He) reduced Cu/ZnO/Al_2O_3 catalysts recorded at ambient temperature. The inset shows the real amplitude of the 1st Cu–Cu shell (without offset).

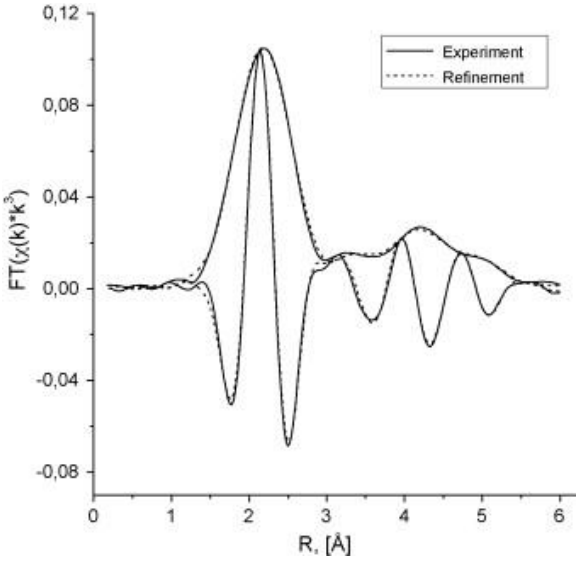

Fig. 9: Refinement of theoretical Cu EXAFS function (dashed line) to the experimental Cu K-edge FT($\chi(k)\cdot k^3$) (solid line) of CZA-1 catalyst after MSR reaction at 313 K.

with the trend in activity obtained in the *in situ* XRD cell and in the fixed-bed micro reactor (Fig. 1). A structural refinement of a theoretical spectrum of bulk *fcc* Cu to the experimental spectra revealed no shift of the distance of the first copper metal shell which indicates that no additional Cu containing phases, such as brass are detectable in the bulk (Table 4). This is in agreement with the obtained lattice constants of Cu (see Table 4). In Fig. 9 the results of a refinement of a theoretical Cu EXAFS function to an experimental FT($\chi(k)\cdot k^3$) of sample CZA-1 at 313 K after MSR reaction conditions is depicted. A good agreement between

Table 5: Structural parameters obtained from refinement of theoretical *fcc* copper metal to the experimental Cu K-edge EXAFS function recorded after MSR reaction at 313 K (k = 3–13 $Å^{-1}$; R = 1.7–6 Å; Refinement includes 5 single and 9 multi scattering paths; N_{ind} = 27; N_{free} = 11)

Sample	Shell	CN[a]	R (Å)	σ^2 ($Å^2$)	$\Delta\sigma_{foil}{}^2$ ($Å^2$)
CZA-1	1. Cu–Cu	12	2.53(4)	0.0110	−0.0009
	2. Cu–Cu	6	3.62(2)	0.0171	−0.0013
	3. Cu–Cu	24	4.41(7)	0.0173	−0.0029
	4. Cu–Cu	12	5.08(0)	0.0273	−0.0050
	5. Cu–Cu	24	5.78(0)	0.0315	−0.0065
CZA-2	1. Cu–Cu	12	2.53(4)	0.0116	−0.0015
	2. Cu–Cu	6	3.61(6)	0.0183	−0.0025
	3. Cu–Cu	24	4.40(7)	0.0182	−0.0038
	4. Cu–Cu	12	5.07(2)	0.0275	−0.0052
	5. Cu–Cu	24	5.74(7)	0.0317	−0.0067
CZA-3	1. Cu–Cu	12	2.53(7)	0.0108	−0.0007
	2. Cu–Cu	6	3.63(6)	0.0171	−0.0013
	3. Cu–Cu	24	4.41(6)	0.0169	−0.0025
	4. Cu–Cu	12	5.08(1)	0.0262	−0.0039
	5. Cu–Cu	24	5.76(8)	0.0322	−0.0072
CZA-4	1. Cu–Cu	12	2.54(1)	0.0135	−0.0034
	2. Cu–Cu	6	3.63(6)	0.0196	−0.0038
	3. Cu–Cu	24	4.41(6)	0.0192	−0.0048
	4. Cu–Cu	12	5.08(3)	0.0298	−0.0075
	5. Cu–Cu	24	5.76(8)	0.0367	−0.0116
CZA-5	1. Cu–Cu	12	2.54(0)	0.0127	−0.0028
	2. Cu–Cu	6	3.63(3)	0.0187	−0.0029
	3. Cu–Cu	24	4.42(0)	0.0189	−0.0045
	4. Cu–Cu	12	5.07(9)	0.0310	−0.0087
	5. Cu–Cu	24	5.77(8)	0.0353	−0.0103
CZA-6	1. Cu–Cu	12	2.53(9)	0.0122	−0.0020
	2. Cu–Cu	6	3.62(9)	0.0183	−0.0025
	3. Cu–Cu	24	4.41(8)	0.0183	−0.0039
	4. Cu–Cu	12	5.08(0)	0.0298	−0.0075
	5. Cu–Cu	24	5.78(1)	0.0351	−0.0103

[a] Non-refined parameter (fixed).

experimental and theoretical data can be seen. The structural parameters of the single scattering paths obtained from a refinement of theoretical bulk copper to the experimental Cu K-edge EXAFS for all CZA catalysts studied are summarized in Table 5. The obtained variation of the amplitude of the 1st Cu–Cu shell in Fig. 4 corresponds to a different structural disorder (*Debye–Waller* factor, σ_{Cu}^2) in the Cu within the CZA series. The DWF obtained depends on the Cu crystallite size determined from XRD. The smaller the Cu crystallite size the higher the structural disorder in the Cu phase (Fig. 10). However, two groups of catalysts have been identified: Samples CZA-1–3 on the one and CZA-4–6 on the other hand. Each group exhibits a linear correlation between the obtained DWF and the Cu crystallite size of the Cu(1 1 1) reflection (see Fig. 10). Confidence limit of the DWF of the first Cu–Cu shell was estimated to be about 0.0001 $Å^2$. Hence, error bars in Fig. 10 are in the order of the thickness of the symbols used.

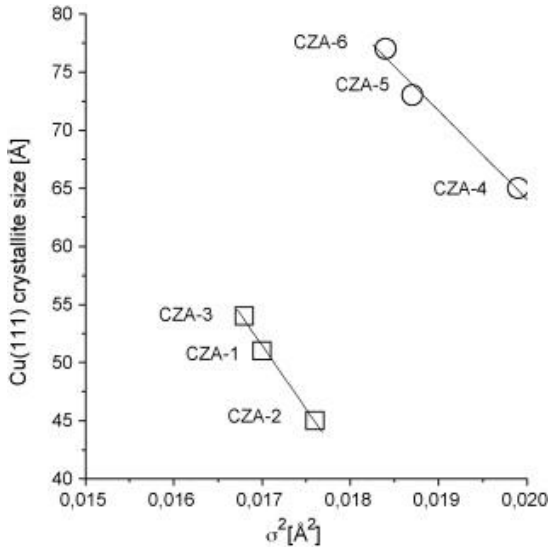

Fig. 10: Correlation of Cu crystallite size (XRD) with the DWF of the 1st Cu–Cu shell (XAS) derived from a refinement of theoretical Cu functions to the experimental data.

In Fig. 11 the FT($\chi(k)\cdot k^3$) measured at the Zn K-edge in reducing atmosphere after the activation procedure at ambient temperature are depicted. The first peak (R = 1–2 Å) attributed to Zn in a distorted tetrahedral coordination by oxygen is also visible for the measured ZnO reference. Differences compared to a crystalline ZnO reference can be seen at distances above 2 Å. For the catalysts investigated the peak at 3 Å attributed to the 1st Zn–Zn shell in a ZnO crystal is diminished relative to the ZnO reference. Apparently, the Zn K-edge EXAFS indicates the presence of a zinc species different from bulk crystalline ZnO. In Fig. 12 the Zn FT($\chi(k)\cdot k^3$) of the calcined CZA-1 precursor is compared to the RDF obtained after reduction in hydrogen. The amplitude of the first zinc metal shell (R = 2.9 Å) of the reduced CZA-1 catalyst was barely half of the first Zn–O

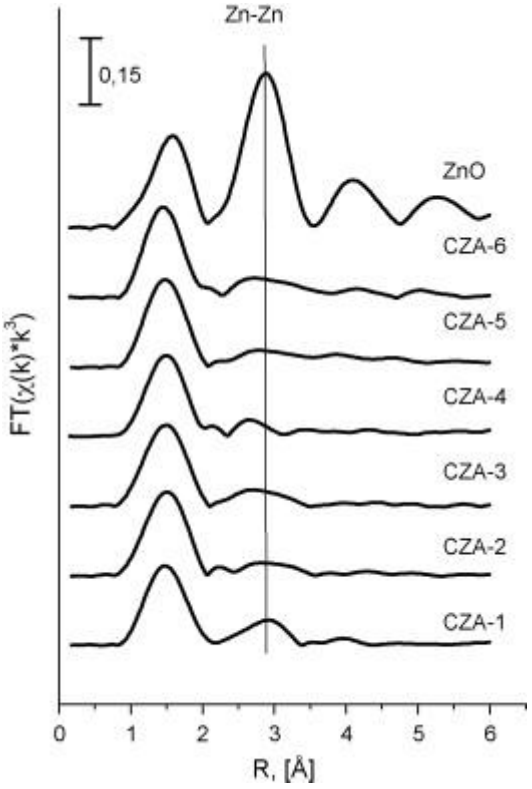

Fig. 11: Experimental FT($\chi(k)\cdot k^3$) of the reduced Cu/ZnO/Al_2O_3 catalysts under reduction conditions recorded at ambient temperature together with the radial distribution function (RDF) of a reference ZnO measured at the Zn K-edge.

peak (R = 1.5 Å). According to the analysis of the evolved gas phase, decomposition of a Zn containing hydroxycarbonate precursor material took place during reduction. A refinement of a theoretical ZnO model structure to the experimental Zn FT($\chi(k)\cdot k^3$) obtained after reduction revealed a highly defect rich ZnO phase for sample CZA-1 (see Fig. 12). Conversely, the refinement of the ZnO model structure to the experimental RDF of samples CZA-2–6 after reduction alone resulted in a high Fit residual. No structural differences in regard to Zn–O as well as Zn–Zn distances and the corresponding DWF's have been found between the reduced catalysts and the catalysts under MSR reaction conditions. Accordingly, the absorption edge position of the Zn K-edge did not change by switching from reduction atmosphere to MSR feed (Table 6).

4. Discussion

4.1. Microstructure of Cu in Cu/ZnO/Al_2O_3 catalysts

The catalysts investigated exhibit considerable differences in MSR activities. This emphasizes the eminent relevance of the catalyst preparation for the electronic and structural properties of the resulting solids (see Fig. 1). Conversions of methanol on the catalysts studied can cer

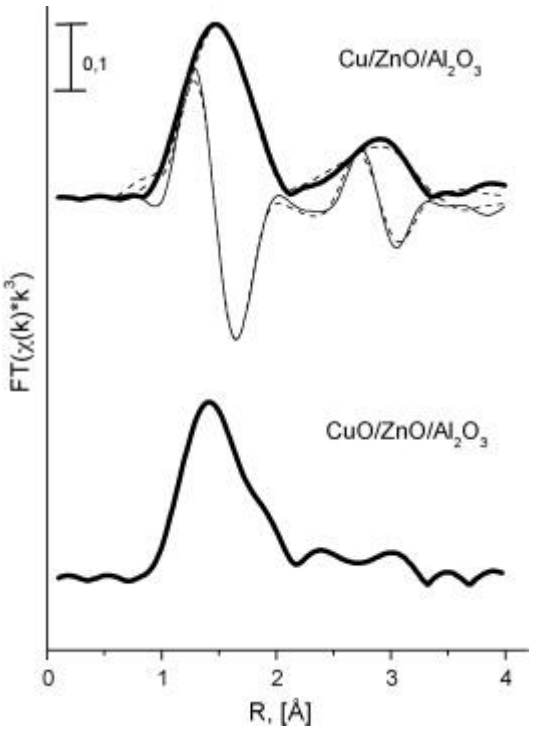

Fig. 12: Experimental Zn K-edge FT($\chi(k)\cdot k^3$) measured before and after reduction in hydrogen of the sample CZA-1: calcined oxide precursor (bottom) and reduced catalyst (top) with refinement of theoretical ZnO EXAFS function (dashed line) to the experimental Zn K-edge FT($\chi(k)\cdot k^3$) (solid line).

tainly be enhanced to the thermodynamic equilibrium by decreasing the space velocity (WHSV). However, an optimization of the catalytic performance with respect to a complete methanol conversion was not the objective of this study. Catalytic performance in MSR is mainly determined by the surface area of the active copper phase (Fig. 2). However, a significant deviation from a linear correlation between copper surface area and activity has been found. This deviation is most pronounced for the samples CZA-2 and CZA-5–6 which exhibits a similar Cu surface area of about 5 $m_{Cu}^2\, g_{cat}^{-1}$ but still differ considerably in the catalytic activity (see Fig. 2). Strained copper particles were detected only for the catalyst CZA-1 which also exhibited the highest specific Cu surface area of all catalysts studied (Table 3). Highest intrinsic activities per m_{Cu}^2 have been found for the sample CZA-2. Catalyst CZA-1 exhibits even less activity per m_{Cu}^2 than the samples CZA-2–5 (see Table 1). Strain appeared to be the consequence of the homogeneous microstructure, high Cu dispersion and a high Cu surface area found in CZA-1. This confirms previous investigations of binary Cu/ZnO catalysts concerning the relevance of bulk structural defects in stabilization of a high Cu surface area in methanol chemistry [10]. Apparently, the deviation from the ideal structure of bulk copper is essential for attaining an improved catalytic performance. The high degree of disorder in the Cu nanoparticles may result from an increased interface area between Cu and ZnO [6], [9], [10], [12], [13], [14] and [21]. This is confirmed by HRTEM investigations of CZA-1 which revealed a variety of both epitaxial and irregular arrangements of, in most cases, relatively smooth Cu–ZnO interfaces (Fig. 5a). The existence of subsurface oxygen at the Cu–O–Zn interface which also has been ascribed to cause disorder in the Cu particles can not ruled out for the Cu/ZnO/Al_2O_3 catalysts investigated [41].

The catalyst CZA-1 exhibited the lowest reduction temperature and a rather narrow and symmetrical TPR peak compared to the other samples. By means of temperature programmed XANES investigations at the Cu K-edge the shoulder which appeared at lower temperature side in the TPR signal was assigned to the appearance of Cu_2O as an intermediate phase during the reduction of Cu(II) to Cu(0) as it was also found for other Cu based mixed oxides [42]. Previous investigations concerning the reducibility of copper based catalysts for methanol synthesis and MSR have revealed that good reducibility is associated with a high activity of the corresponding catalyst [43] and [44]. In addition to the low reduction temperature, the shape of the TPR profile of sample CZA-1 indicates a homogeneous microstructure of small and uniformly distributed copper particles [14]. Conversely, the samples CZA-2–6 exhibit a heterogeneous mixture of large and isolated Cu particles (see Fig. 4 and Fig. 5). The pronounced bimodal particle size distribution of small and large Cu agglomerates (5–150 nm) observed by electron microscopy is also reflected in the TPR profiles. A shift to higher reduction temperatures as well as a pronounced broadening of the reduction peaks indicates large and less dispersed copper particles in those catalysts (see Fig. 3). Apparently, the main fraction of CuO is less accessible to hydrogen during the reduction procedure and therefore may also less accessible to the reactants MeOH and H_2O during MSR reaction. Consistently, the copper surface area calculated from XRD line broadening is much larger than the area determined by RFC. Only for CZA-1 the calculated Cu surface area for all diffraction domains matches the RFC results (Table 3). Deviations found for the samples CZA-2–6 may originate from non-spherical copper particles or from different activities of individual copper lattice planes exposed at the surface. More likely though, it is the agglomeration of copper particles which reduces the accessible Cu surface area. Apparently, the large copper particles in samples CZA-2–6 are composed of mosaic crystals with smaller domains. Thus, the accessible surface area is noticeable lower than the total surface area calculated for all diffraction domains. In opposite to CZA-1 samples CZA-2–6 partially consist of isolated Cu particles in the ZnO/Al_2O_3 matrix (see Fig. 3). Hence, determining the reducibility of the copper species in terms of reduction temperature and reduction profile is well suited as indicator for the catalytic performance of the present Cu/ZnO/Al_2O_3 samples.

The bulk consists of metallic copper which is not transferred into other phases, such as bulk oxides or alloys. This indicates that metallic copper is the active phase. Conversely, an increasing Cu–Zn(ZnO_{1-x}) alloying abundance in the bulk is accompanied by a decrease in MSR activity

Table 6: Zn K-edge position (E_0) of the calcined precursor (313 K), the reduced catalyst (523 K), and the catalyst under MSR conditions (523 K)

Sample	E_0 ZnO (keV)		
	Calcined	Reduced	In MSR feed
CZA-1	9.658(5)	9.662(3)	9.662(4)
CZA-2	9.658(8)	9.662(8)	9.662(7)
CZA-3	9.658(4)	9.662(9)	9.662(9)
CZA-4	9.658(8)	9.662(4)	9.662(2)
CZA-5	9.658(6)	9.663(2)	9.663(0)
CZA-6	9.658(6)	9.662(9)	9.662(7)

[14]. Consistently, no variations in lattice cell parameters (XRD) and in distance of the 1st Cu–Cu shell (XAS) of Cu were observed for all samples. Hence, Cu/Zn solid solutions were not detectable in the bulk (Table 4). Conversely, HRTEM investigations confirmed the presence of minute amounts of Cu_2O and brass in the reduced Cu/ZnO/Al_2O_3 catalysts. These may originate from traces of oxygen during glove box transfer or incomplete reduction.

The averaged crystallite sizes determined by X-ray diffraction line profile analysis and particle sizes obtained from TEM investigations classify copper as a nano-crystalline material. These copper particles exhibit a certain disorder in short and medium range order as it can be deduced from the high *Debye–Waller* factor (DWF) of copper compared to *ideal* bulk copper (Table 4 and Table 5). The differences of the DWF observed within the series of CZA catalysts did not coincide with the calculated lattice strain in the Cu crystallites. Apparently, the observed variation in amplitude of the single scattering Cu–Cu shells is mainly caused by size effects (Fig. 10). Generally, the temperature independent (static) disorder is increased in a nano-crystalline sample with respect to macro-crystalline bulk like particle. The elevated static disorder reflects an incoherent bond length distribution within the nano-crystals [45]. Two groups of catalysts which have been identified exhibit a different dependency of the DWF on the Cu crystallite size. Apparently, the less active samples CZA-4–6 exhibit more structural disorder in the Cu crystallites under MSR reaction conditions than samples CZA-1–3 (Fig. 10). However, the different dependencies observed within the CZA series did not coincide with the catalytic performance of the catalysts investigated. Only samples CZA-4–6 exhibit a linear correlation between static structural disorder in the Cu lattice obtained from *in situ* XAS studies and the measured activity in the *in situ* cell. Those samples have been prepared in equal manner. Apparently, this trend is caused by the observed specific Cu surface area of these catalysts. The determined Cu crystallite sizes of samples CZA-4–6 coincide with the measured Cu surface area and are also reflected in the catalytic activity (see Table 3). Conversely, samples CZA-1–3 did not show this dependency indicating that the observed DWF contained complex information which strongly depends on the kind of preparation of the catalyst.

Crystallites which are significantly smaller than 10 nm exhibit a high fraction of surface atoms relative to the bulk. Accordingly, due to inharmonic, non-Gaussian pair distribution function the RDF will result in a reduction in the averaged coordination number [46]. During the fit procedure employed, the coordination numbers of Cu were kept constant at the values of bulk copper (CN = 12). The copper crystallite sizes of the Cu/ZnO/Al_2O_3 catalysts studied range from 5 nm to 8 nm (Table 3). Thus, both geometric effects due to the nano-sized Cu crystallites and structural disorder may account for the reduction in amplitude observed for 1st Cu–Cu shell (Fig. 8). However, an EXAFS refinement with the *Debye–Waller* factor fixed to those of Cu bulk afforded an apparent coordination number of 8–9 for copper. Here the coordination number is treated as a fitting parameter with DWF's fixed to those of Cu foil measured as reference. Based on molecular dynamics simulations averaged coordination numbers of nano-sized copper with an crystallite size of 5–8 nm has been calculated to be 11–11.5 [47]. The considerably lower coordination number of Cu (CN = 8–9) determined form experimental EXAFS indicates that a high fraction of Cu atoms located on the surface with respect to the bulk only play a minor role for the observed reduction of the amplitude in the RDF. Accordingly, the measured Cu surface area as result of a more or less pronounced dispersion of Cu (Table 3) is not reflected in the observed variation of the amplitude in the radial distribution function. Both geometric effects due to reduction in the CN to a minor and (static) structural disorder in the copper crystallites to a major part account for the observed reduction of the amplitude in the FT($\chi(k)$) in a cumulative manner.

4.2. Microstructure of ZnO and Al_2O_3 in Cu/ZnO/Al_2O_3 catalysts

The role of ZnO in copper based catalysts for methanol chemistry has been controversially debated in the literature. Apparently, ZnO prevents Cu sintering and remove catalyst poisons (i.e. sulfides and halogenides) under working conditions in methanol synthesis as well as steam reforming [24] and [48]. In semi-conductor science it is well established that the electronic properties of highly defective, nano-scaled zinc oxide, such as the band gap size, significantly differ those of macro-crystalline ZnO [49]. Decomposition of appropriate CuZn(Al)-hydroxycarbonates is believed to result in a particular zinc oxide modified by ad-mixed OH^- and CO_3^{2-} groups [50]. Such a modified zinc oxide serves as a growth inhibitor of copper particles [25], [51] and [52]. Hence, mild reduction in hydrogen results in copper dissolved in ZnO and copper metal particles bonded epitaxially to the surface of the ZnO

matrix [50]. EXAFS investigations of various calcined $CuO/ZnO/Al_2O_3$ precursors at the Zn K-edge indicated the presence of zinc phases different from ZnO. This indicates the presence of additional Zn species other than ZnO in the non-reduced catalyst state (Fig. 12). The increase in XAS amplitude of the 1st Zn–Zn shell of sample CZA-1 during reduction implies that ZnO undergoes a microstructural ordering in the medium range structure (Fig. 12). Consistently, the determined Zn K-edge position shifted of about 4 eV during reduction with respect to the calcined sample (Table 6). Analysis of the MS data revealed that the observed shift in the Zn K-edge position during reduction coincides with a release of H_2O and CO_2. Consistently, the Rosasite reflections found in the CZA-1 oxide precursor disappeared in reduced catalyst (Fig. 6). After reduction *in situ* XRD investigations exhibited crystalline ZnO with a crystallite size of about 39 Å for CZA-1 (Fig. 6b). Additionally, electron microscopy investigations on the sample CZA-1 confirmed a highly defect rich microstructure of crystalline ZnO including dislocations, bent lattice planes, and a rough surface morphology. ZnO appeared nearly spherical shaped with an averaged diameter of $d_{ZnO} \approx 7$ nm (Fig. 5a). However, the presence of oxygen deficit ZnO which has been found in rare cases by HRTEM investigations has not been confirmed by analysis of the Zn K-edge position in the reduced state as well as under MSR reaction conditions (Table 6). This indicates that either the abundance of ZnO_{1-x} is negligible in the CZA-1 catalysts or that the absorption K-edge of Zn is dominated by different Zn^{2+} species. The short-range order structure (<2 Å) of this resulting ZnO phase mainly corresponds to disordered ZnO. Hydroxide and carbonate species may persist after mild thermal treatment (calcination, reduction) in the catalytically active catalyst [25]. Thus, the diminished amplitude of the 1st Zn–Zn shell obtained after reduction of sample CZA-1 may be caused by a superimposition of the spectra of different Zn species in addition to a highly disordered ZnO phase (Fig. 12). The presence of these species located at the zinc centers should result in a modified microstructure at the Zn–O–Cu interface which causes the detected lattice strain in the copper nanoparticles [50]. Conversely, the presence of crystalline Hydroxycarbonates has not been confirmed by XRD for the reduced CZA-1 (Fig. 6b). Apparently, Zn K-edge EXAFS probes the amorphous part of the catalysts which is not observable by XRD. Consistently, TEM revealed the presence of amorphous structures in the reduced CZA-1 catalyst.

EXAFS spectra at the Zn K-edge of the samples CZA-2–6 show no microstructural changes like that of sample CZA-1 during reduction in hydrogen (Fig. 11). In good agreement with these results, no long range ordered ZnO phase was detectable by X-ray diffraction. Consistently, HRTEM investigations did not reveal the presence of nano-crystalline ZnO sticks to Cu particles as it was found for CZA-1. Typically, Cu particles are embedded in an amorphous matrix which shapes large plate- or needle like structures (see Fig. 4 and Fig. 5). Apparently, even after reduction in hydrogen, "ZnO" remains in an amorphous state similar to that of the calcined precursors. Thus, differences found in RDF with respect to CZA-1 are most probably due to an unfavored texture of ZnO in samples CZA-2–6. In contrast to CZA-1, the diminished amplitude of the 1st Zn–Zn shell obtained after reduction may be caused by a highly amorphous texture of ZnO. The pronounced loss of structural coherence above 2 Å in the Zn K-edge $FT(\chi(k)\cdot k^3)$ corresponds to a highly amorphous texture of ZnO in these catalysts [53]. The highly non-ordered character of ZnO in the bulk of catalysts CZA-2–6 is confirmed by *in situ* XRD (Fig. 6). Consistently, TEM investigations exhibit a less pronounced nano-structuring of intimately mixed ZnO and Cu particles with respect to CZA-1 (Fig. 4 and Fig. 5). In consequence of that, samples CZA-2–6 exhibited Cu surface areas of less than 9 $m_{Cu}^{-2}\, g_{Cat}^{-1}$ (Table 3). Apparently, ZnO is required to maintain the active copper phase in optimal dispersion without allowing segregation. Thus, ZnO is not just a support but integral part of the active copper based catalyst. The bulk structure and, hence, the catalytically active surface is determined by an advanced Cu/ZnO interface.

Alumina does not appear as a separate phase detectable by X-ray diffraction and TEM investigations. Only in rare cases Al has been identified as crystalline α-Al_2O_3 by HRTEM. Cu–Al interactions in $Cu/ZnO/Al_2O_3$ catalysts have been suggested by Figueiredo et al. [54]. However, the addition of aluminum in the precipitation process significantly changes the precursor chemistry according to the structural and electronic properties of ternary $Cu/ZnO/Al_2O_3$ compared to binary Cu/ZnO catalysts. Thus, superior activities have been described for $Cu/ZnO/Al_2O_3$ catalysts exhibiting a similar copper surface area like comparable Cu/ZnO catalysts [55] and [56].

4.3. Thermal stability of $Cu/ZnO/Al_2O_3$ catalysts

Copper metal exhibits a low *Tammann* temperature corresponding to a low melting point of $T_M = 1356$ K [57]. Therefore, $Cu/ZnO/Al_2O_3$ catalysts suffer from thermal deactivation by sintering at temperatures above 673 K. Thermal stability of copper based catalysts strongly depends on both the preparation procedures used and the chemical composition [24]. Hence, the catalyst preparation is a crucial point since thermal degradation can be limited in well-formulated catalysts prepared under optimized conditions [48]. During *in situ* reduction of the catalysts sintering occurred for the samples CZA-2–6 resulting in an increase in Cu crystallite sizes compared to crystallite sizes of the corresponding oxides (Fig. 7). Sintering accompanied by loss of Cu surface area is highly pronounced for the samples CZA-5 and CZA-6 and is reflected in a poor hydrogen production rate obtained in MSR (see Table 1). Degradation is less pronounced for the samples CZA-2, and 3 (Fig. 7). Subsequent exposure to MSR conditions caused no further sintering indicating that the reduction process is the decisive step in catalyst activation [58]. The commercial CZA-1 catalyst exhibited no sintering neither during

the reduction process nor under MSR working conditions. Apparently, the tendency for sintering depends on the interaction of copper particles and the ZnO/Al_2O_3 matrix. Thus, we conclude that the enhanced stability for the commercial $Cu/ZnO/Al_2O_3$ catalysts compared to the laboratory prepared catalysts in methanol steam reforming reaction is closely related to the increased structural disorder (lattice strain) in the Cu particles. Lattice strain in the copper particles is a consequence of the nano-structuring of Cu and ZnO. The latter keeps the Cu crystallites in a meta-stable state and thus maintains a high active surface area. While maintaining a similar copper surface area, the strained CZA sample revealed a significantly increased thermal stability in methanol steam reforming reaction.

The superior activities obtained for ternary $Cu/ZnO/Al_2O_3$ catalysts compared to binary Cu/ZnO catalysts with a similar copper surface area may be originating from the more complex precursor chemistry of these catalysts during the precipitation process [56]. Addition of aluminum as a third cationic component will change the electronic and structural properties of the final catalyst and may result in an enhanced activity. Nevertheless, structural and catalytically relevant differences obtained from the binary Cu/ZnO model system can be reliably extrapolated to $Cu/ZnO/Al_2O_3$ catalysts. Correlations found for the binary system [6], [10], [12], [13] and [14], such as phase composition, reduction characteristics, crystallinity, homogeneity of microstructure and structural disorder are also valid for the more complex $Cu/ZnO/Al_2O_3$ system.

5. Summary

Various ternary $Cu/ZnO/Al_2O_3$ catalysts were tested for methanol steam reforming activity. Consistent with previous investigations of binary Cu/ZnO model systems, the hydrogen production rate exhibited no linear correlation with the specific copper surface area. The catalytic activity and thermal stability under MSR reaction conditions was also influenced by structural defects in the bulk of the materials. Lattice strain in the copper particles is a consequence of the nano-structuring of Cu and ZnO. ZnO keeps the Cu crystallites in a meta-stable state and thus maintains a high active surface area.

Differences in the microstructure obtained for the $Cu/ZnO/Al_2O_3$ has been also found for binary Cu/ZnO model system. Thus, structure–activity correlations drawn for the binary system such as phase composition, reduction characteristics, crystallinity, homogeneity of microstructure and structural disorder are also valid for *real* $Cu/ZnO/Al_2O_3$ catalysts. Therefore, specific microstructural characteristics in addition to a high copper surface area have to be achieved for appropriate Cu catalysts for methanol steam reforming. Adjusting a suitable microstructure on the basis of binary Cu/ZnO model system will help to yield advanced $Cu/ZnO/Al_2O_3$ catalysts and will eventually provide the basis for a rational catalyst design.

Acknowledgements

Norbert Pfänder is acknowledged for conducting TEM measurements. The Hamburg Synchrotron Radiation Laboratory, HASYLAB, is acknowledged for providing beamtime for this work. Furthermore, the authors gratefully acknowledge the German Bundesministerium für Bildung und Forschung (BMBF project number: 01RI05029) for financial support.

References

[1] P.J. de Wild and M.J.F.M. Vernaak, *Catal. Today* **60** (2000), p. 3.
[2] C. Lamy, A. Lima, V. LeRhun, F. Delime, C. Counteaceau and J.M. Léger, *J. Power Sources* **105** (2002), p. 283.
[3] M. Krumpelt, T. Krause, J.D. Carter, J.P. Kopasz and S. Ahmed, *Catal. Today* **77** (2002), p. 3.
[4] Y.M. Lin and M.H. Rei, *Int. J. Hydrogen Energy* **25** (2000), p. 211.
[5] K.C. Waugh, *Catal. Lett.* **58** (1999), p. 163.
[6] M.M. Günther, T. Ressler, R.E. Jentoft and B. Bems, *J. Catal.* **203** (2001), p. 133.
[7] M. Kurtz, H. Wilmer, T. Genger, O. Hinrichsen and M. Muhler, *Catal. Lett.* **86** (2003), p. 77.
[8] J. Agrell, H. Birgersson, M. Boutonnet, I. Melian-Cabrera, R.M. Navarro and J.L.G. Fierro, *J. Catal.* **219** (2003), p. 389
[9] X.R. Zhang, L.C. Wang, Y. Cao, W.L. Dai, H.Y. He and K.N. Fan, *Chem. Commun.* **32** (2005), p. 4104.
[10] M.M. Günther, T. Ressler, B. Bems, C. Büscher, T. Genger, O. Hinrichsen, M. Muhler and R. Schlögl, *Catal. Lett.* **71** (2001), p. 37.
[11] F. Girgsdies, T. Ressler, U. Wild, T. Wübben, T.J. Balk, G. Dehm, L. Zhou, S. Günther, E. Arzt, R. Imbihl and R. Schlögl, *Catal. Lett.* **102** (2005), p. 91.
[12] B.L. Kniep, T. Ressler, A. Rabis, F. Girgdies, M. Baenitz, F. Steglich and R. Schlögl, *Angew. Chem. Int. Ed.* **43** (2004), p. 112.
[13] T. Ressler, B.L. Kniep, I. Kasatkin and R. Schlögl, *Angew. Chem. Int. Ed.* **44** (2005), p. 4704.
[14] B.L. Kniep, F. Girgdies and T. Ressler, *J. Catal.* **236** (2005), p. 34.
[15] K. Klier, *Adv. Catal.* **31** (1982), p. 243.
[16] G.C. Chinchen, K.C. Waugh and W. Da, *Appl. Catal.* **25** (1986), p. 101.
[17] R. Burch, S.E. Golunski and M.S. Spencer, *J. Chem. Soc. Faraday Trans.* **86** (2000), p. 1990.
[18] T. Fujitani and J. Nakamura, *Catal. Lett.* **56** (1998), p. 119.

[19] N.Y. Topsøe and H. Topsøe, *J. Mol. Catal. A* **141** (1999), p. 95.
[20] M.S. Spencer, *Catal. Lett.* **66** (2000), p. 255.
[21] J.B. Wagner, P.L. Hansen, A.M. Molenbroek, H. Topsøe, B.S. Clausen and S. Helveg, *J. Phys. Chem. B* **107** (2003), p. 7753.
[22] S. Velu, K. Suzuki and T. Osaki, *Catal. Lett.* **62** (1999), p. 159.
[23] J. Breen and R.H. Ross, *Catal. Today* **51** (1999), p. 521.
[24] M.V. Twigg and M.S. Spencer, *Appl. Catal. A* **212** (2001), p. 161.
[25] B. Bems, M. Schur, A. Dassenoy, H. Junkes, D. Herein and R. Schlögl, *Chem. Eur. J.* **9** (2003), p. 2039.
[26] A.B. Stiles, German Patent, DE 2320 192 (1973), to DuPont company.
[27] H. Fukui, M. Kobayashi, T. Yamaguchi, H. Arakawa, K. Okabe, K. Sayama, H. Kusama, European Patent, EP 0 868 943 B1 (2002), to YKK cooperation.
[28] G.C. Chinchen, K.C. Waugh and W. Da, *J. Catal.* **103** (1987), p. 79.
[29] O. Hinrichsen, T. Genger and M. Muhler, *Chem. Eng. Technol.* **23** (2000), p. 11.
[30] R.M. Dell, F.S. Stone and P.F. Tiley, *Trans. Faraday Soc.* **49** (1953), p. 195.
[31] D.A.M. Monti and A. Baiker, *J. Catal.* **83** (1983), p. 323.
[32] P. Malet and A. Caballero, *J. Chem. Soc. Trans. Faraday Trans. 1* **84** (1988), p. 2369.
[33] G.S. Pawley, *J. Appl. Cryst.* **14** (1981), p. 357.
[34] P. Scardi, M. Leoni and R. Delhez, *J. Appl. Cryst.* **37** (2004), p. 381.
[35] T. Ressler, *J. Syn. Rad.* **5** (1998), p. 118.
[36] A.L. Ankudinov, B. Ravel, J.J. Rehr and S.D. Conradson, *Phys. Rev. B* **58** (1998), p. 7565.
[37] H. Purnama, T. Ressler, R.E. Jentoft, H. Soerijanto, R. Schlögl and R. Schomäcker, *Appl. Catal. A* **259** (2004), p. 83.
[38] Y. Choi and H.G. Stenger, *Appl. Catal. B* **38** (2002), p. 259.
[39] In: R.C. Weast, Editor, *Handbook of Chemistry and Physics* (57th edition), CRC Press Inc., Cleveland (1976).
[40] S. Velu, K. Suzuki, M. Okazaki, M.P. Kapoor, T. Osaki and F. Ohashi, *J. Catal.* **194** (2000), p. 337.
[41] I. Böttger, T. Schedel-Niedrig, O. Timpe, R. Gottschall, M. Hävecker, T. Ressler and R. Schlögl, *Chem. Eur. J.* **6** (2000), p. 1870.
[42] M.M. Günther, B. Bems, R. Schlögl and T. Ressler, *J. Syn. Rad.* **8** (2001), p. 619.
[43] G. Fierro, M.L. Jacono, M. Inversi, P. Porta, F. Cioci and R. Lavecchia, *Appl. Catal.* **76** (1991), p. 117.
[44] Y. Kawamura, K. Yamamoto, N. Ogura, T. Katsumata and A. Igarashi, *J. Power Sources* **150** (2005), p. 20.
[45] J. Rockenberger, L. Tröger, A.L. Rogach, M. Tischer, M. Grundmann, A. Eychmüller and H. Weller, *J. Chem. Phys.* **108** (1998), p. 7807.
[46] B.S. Clausen, L. Grabek, H. Topsoe, L.B. Hansen, P. Stolze, J.K. Nørskov and O.H. Nielsen, *J. Catal.* **141** (1993), p. 368.
[47] B.S. Clausen and J.K. Nørskov, *Topics Catal.* **10** (2000), p. 221
[48] M.V. Twigg and M.S. Spencer, *Topics Catal.* **22** (2003), p. 191.
[49] V. Ischenko, S. Polarz, D. Grote, V. Stavarche, K. Fink and M. Driess, *Adv. Func. Mater.* **15** (2005), p. 1945.
[50] M. Yurieva, L.M. Plyasova, V.I. Zaikovskii, T.P. Minyukova, A. Bliek, J.C. van den Heuvel, L.P. Davydova, I. Molina, M.P. Demeshkina, A.A. Khassin and E.D. Batyrev, *Phys. Chem. Chem. Phys.* **6** (2004), p. 4522.
[51] G.C. Chinchen, P.J. Denny, J.R. Jennings, M.S. Spencer and K.C. Waugh, *Appl. Catal.* **36** (1988), p. 1.
[52] M.S. Spencer, *Topics Catal.* **8** (1999), p. 259.
[53] B. Gilbert, F. Huang, H. Zhang, G.A. Waychunas and J.F. Banfield, *Science* **305** (2004), p. 651.
[54] R.T. Figueiredo, A. Martinez-Arias, M.L. Granados and J.L.G. Fierro, *J. Catal.* **178** (1998), p. 146.
[55] M. Kurtz, N. Bauer, H. Wilmer, O. Hinrichsen and M. Muhler, *Chem. Ing. Tech.* **76** (2004), p. 42.
[56] M. Kurtz, N. Bauer, C. Büscher, H. Wilmer, O. Hinrichsen, R. Becker, S. Rabe, K. Merz, M. Driess, R.A. Fischer and M. Muhler, *Catal. Lett.* **92** (2004), p. 49.
[57] J.A. Moulijn, A.E. van Diepen and F. Kapteijn, *Appl. Catal. A* **212** (2001), p. 3.
[58] S. Fujita, S. Moribe, Y. Kanamori and N. Takezawa, *React. Kinet. Catal. Lett.* **70** (2000), p. 11.